Adoption of the Synchronous Reluctance Motor in Electric Vehicles: A Focus on the Flux Weakening Capability

Andrea Credo, Marco Villani, Giuseppe Fabri, *Member, IEEE*, and Mircea Popescu, *Fellow, IEEE*

***Abstract*— This article presents the definition of the performance that the electric motor should have in order to satisfy the requirements of the electric vehicle in terms of acceleration time and maximum speed, starting from a simplified vehicle model, considering the motor torque minimization and the input power minimization. In order to verify the effectiveness of the synchronous reluctance motor in traction applications, it has been evaluated in two case studies: a high-performance vehicle and a city car, where different flux weakening capabilities from the motor in function of the minimization strategies can be pursued to satisfy the requirements. If the car requires high performance in terms of acceleration time and maximum speed, the poor flux weakening capabilities of the synchronous reluctance motor induces a machine oversizing in terms of peak power; by assuming this, it is, however, possible to satisfy the requirements considering the maximum available encumbrance due to an advanced and innovative optimized design procedure. The motor of the city car is obtained only by modifying the stack length and the windings (scaled version), and on this last solution, a prototype has been realized and fully tested; the experimental tests confirm the results of the simulations.**

***Index Terms*— Asymmetric rotor, electric vehicles (EVs), high speed, optimization, synchronous reluctance motor (SynRel), topology optimization (TO), traction application.**

I. Introduction

ICE vehicles are still one of the most relevant sources of air pollutants, such as carbon monoxide (CO), black carbon (BC), fine particulate matter, and nitrogen oxides (NO_x), and these emissions are dangerous to people's health. The use of electric vehicles (EVs) may be beneficial for pollutant reduction [1], and the global EV outlook [2] reports that the electric car market has been having a high increase in sales compared to the ones of ICE cars. Indeed, a 40% year-on-year increase has been registered, suggesting that EV production will quickly enter in a large mass scenario. One of the main EV components is the electric machine or motor, where different technology and topologies have been explored. Nevertheless, nowadays, solutions based on Rare Earth (RE) permanent magnets, such as permanent magnet synchronous motor (PMSM) or permanent magnet-assisted synchronous reluctance motors (PMASynRel), are mainstream (Table I).

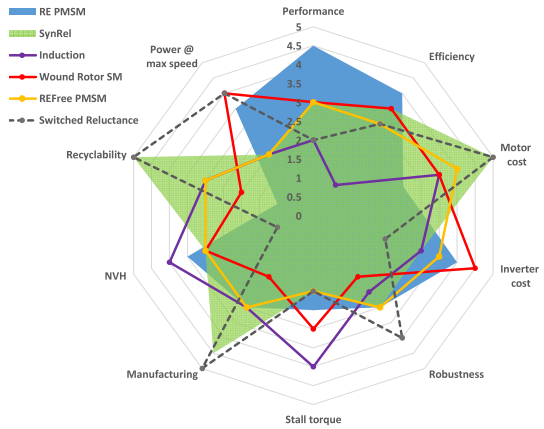

Fig. 1. Main characteristics of electric motors suitable for EV application.

These motors offer the best performance for traction applications thanks to their high power density, high specific torque, high power factor, high efficiency, and good flux weakening capability. All these characteristics are relevant for vehicle application to minimize the material mass (thus increasing dynamic performance), to reduce the size of the power electronics unit, and to reduce energy losses. However, RE magnet-based solutions have to face with an unstable and risky supply chain, leading to high volatility prices. Indeed, a recent JRC study [3] specifies that the European Union (EU) could become vulnerable for the supply of several key materials, including RE, not only relevant in the EV production but also in other technology such as wind turbines.

In this article, the designers are exploring solutions without RE permanent magnets [4], referring to different motor technologies featuring the absence of magnets. In this article, the induction motor [5], [6], [7] and the synchronous reluctance motor (SynRel) [8], [9] are possible candidates for the next generation of electric motors for traction applications.

A sketch of the properties of the most promising radial motor technologies envisioned in traction application is presented in Fig. 1 [10]. Synchronous motors based on

Manuscript received 3 February 2022; revised 28 May 2022; accepted 21 August 2022. Date of publication 5 September 2022; date of current version 21 February 2023. This work was supported by the European Union's Horizon 2020 Research and Innovation Programme through ReFreeDrive under Grant 770143. *(Corresponding author: Andrea Credo.)*

Andrea Credo, Marco Villani, and Giuseppe Fabri are with the Department of Industrial and Information Engineering and Economics, University of L'Aquila, 67100 L'Aquila, Italy (e-mail: andrea.credo@univaq.it; marco.villani@univaq.it; giuseppe.fabri@univaq.it).

Mircea Popescu is with Ansys, LL13 7YT Wrexham, U.K. (e-mail: mircea.popescu@ansys.com).

Digital Object Identifier 10.1109/TTE.2022.3204435

TABLE I
TRACTION MOTORS FOR EVS (2020–2021) [11]

Vehicle Model	Motor type Front / Rear	Max Power (kW) Front / Rear	Top speed (km/h)	Acceleration 0-100 km/h (s)	Transmission ratio	EM Max speed (rpm)	Battery energy (kWh)
Audi e-tron 55	IM / IM	125 / 140	200	6.6	9.2	13000	97
BMW i3S 33/42	- / PMASynRel	- / 135	160	7.0	9.66	11500	33.2/42.2
FIAT 500e	PMSM / -	83 /-	141	-	9.59	12000	24
Hyundai e-Kona 39	PMSM / -	100 / -	155	9.7	7.98	10000	39
Hyundai e-Kona 64	PMSM / -	150 / -	167	7.6	7.98	10500	64
Jaguar I-Pace	PMSM / PMSM	147 / 147	200	4.8	9.04	13000	100
KIA e-Niro 4	PMSM / -	150 / -	167	7.8	8.21	11000	64
KIA Soul EV 39	PMSM / -	100 / -	156	8.21	8.21	10400	39
KIA Soul EV 64	PMSM / -	150 / -	167	7.6	8.21	11000	64
Mercedes-Benz EQC	IM / IM	300 (Total)	180	5.1	-	-	80
MINI Cooper SE	PMSM / -	135 / -	150	7.3	3.07	4000	32.6
Opel Mokka-e	PMSM / -	100 / -	150	9	8.5	10300	50
Opel Corsa-e	PMSM / -	100 / -	150	8.1	8.5	10300	50
Porsche Taycan 4S	PMSM / PMSM	160 / 160	250	4.1	-	-	79.2
Porsche Taycan Turbo	PMSM / PMSM	160 / 300	260	3.2	-	-	93.4
Renault Twingo EL	PMSM / -	60 / -	135	12.9	9.5	11000	22
Renault Zoe R135	PMSM / -	100 / -	140	9.9	9.5	11500	54.66
ŠKODA CITIGOe	PMSM / -	61 / -	130	12.5	9.6	11000	36.8
Tesla Model 3	IM / PMASynRel	147 / 211	261	3.3	9	17000	79.5
Tesla Model X	PMASynRel / IM	205 / 375	261	2.8	9.73 / 9.33	18000	100
Tesla Model Y	IM / PMASynRel	340 (Total)	250	3.7	9.1	16500	74
Tesla Model S	PMASynRel / IM	147 / 211	261	2.5	9.73 / 9.3	18000	100
Volkswagen e-Golf	PMSM / -	100 / -	150	9.6	9.7	12000	35.8
Volkswagen e-up!	PMSM / -	60 / -	130	12.4	8.16	10000	18.7
Volkswagen ID.3	- / PMSM	- / 107	160	9.6	-	-	58
Volkswagen ID.4	- / PMSM	- / 150	160	8.5	-	-	77
Volvo XC40	PMSM / PMSM	150 / 150	180	4.9	-	-	78

PMSM = PM Synchronous Motor; IM = Induction Motor; PMASynRel = Permanent Magnet Assisted Synchronous Reluctance Motor; WRSM = Wound Rotor Synchronous Motor

RE magnets are effective, where dynamic performances and efficiency are demanded. Nevertheless, other motor technologies seem more suitable on the recyclability aspects. RE-free magnet can improve recyclability penalizing the performance and the efficiency. Among the PM-free technologies, induction motors are particularly interesting for the high stall torque, while the poor efficiency may penalize the vehicle range. There is a renewed interest on the wound rotor synchronous motors, where the potentially wide speed range faces rotor windings integrity issues. Synrels and switched reluctance motors are potentially low cost and ease of manufacturing since the rotors are made by electrical steel only.

Each vehicle segment requires different motor characteristics, where the general considerations on the pros and cons of each motor technology need to be specifically analyzed with proper design refinements and system level evaluations. In this article, the aim of this article is the verification of the possible adoption of the SynRel in traction application evaluating two vehicle segments example.

In particular, the SynRel motor technology is quite attractive due to the absence of magnets or windings inside its rotor core, making it a potentially cost-effective solution. The SynRel motor has lower costs compared most of the other motor technologies, both for the raw materials that it uses (the rotor is made only of electrical steel) and for its manufacturing process, since it does not require the insertion of RE permanent magnets, windings, or a cage in the rotor. However, SynRels have lower efficiency and power factor compared to

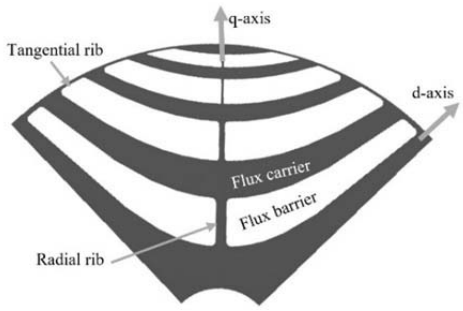

Fig. 2. Typical geometry of the SynRel rotor with flux barriers and ribs.

RE PM motors and higher system costs have to be afforded to increase the battery size and the power electronics capabilities. Therefore, even if the SynRel seems not to be cost-effective at the vehicle level today, the perspectives of a cost reduction of the batteries and the criticalities in the supply of RE materials can foster the adoption of SynRel technology. A sketch of the rotor core with its main elements is shown in Fig. 2.

This motor typology is not penetrating in EV traction applications due to its weak performance in terms of power density, specific torque, and power factor. The gap toward RE-PM motors is filled by accurate design procedures [12], [13], [14] and by increasing the motor operating speed.

The aim of this article is to investigate the adoption of SynRel motors in EVs as a competitive alternative to

RE-PM motors, focusing on the impact of the requirements of the EV application in terms of acceleration and vehicle speed on the SynRel motor design. To this extent, in Section II, a strategy to determine the SynRel requirements from the vehicle requirements by using a simplified vehicle model is proposed. In Section III, two case studies are presented and the proposed methodologies are applied. Section IV reports the highlights of the motor design procedure carried out to match the requirements, and the prototype and the experimental validation of the procedure are presented in Section V. Finally, Section VI presents and discusses the conclusions. The research activity was partially carried out within the H2020 European Project ReFreeDrive [10].

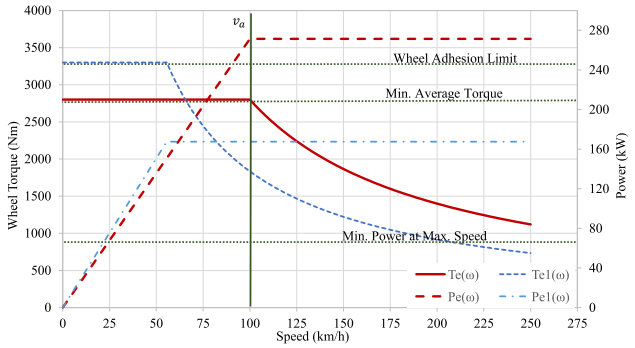

Fig. 3. Ideal torque–speed characteristics of an EV.

II. SynRel Requirements Definition Based on Vehicle Performance

A vehicle is a very complex system that is difficult to be represented by a comprehensive model that is also effective to be used in the definition of the powertrain's requirements and in the preliminary estimation of the vehicle performance [15]. To this purpose, there are several models for the computation of the vehicle kinematics and dynamics [16], [17], [18], [19], but the most adopted one is the longitudinal dynamic model, in which the vehicle is modeled as a point mass where the main forces act [20]. The wheels' friction, the aerodynamic drag, and the gravity force are considered in the model and balanced by the traction force and torque with respect to the wheel-road contact point as described by the following equation:

$$\begin{cases} F_T - F_R = m_{\text{eq}} \dfrac{dv}{dt} \\ T - F_R r = J_{\text{eq}} \dfrac{d\omega}{dt} \end{cases} \tag{1}$$

where F_T is the traction force exchanged at the wheel's contact surface, F_R is the resistance force, T is the motion torque, r is the radius of the wheel, v is the linear speed, ω is the angular speed, m_{eq} is the equivalent mass, and J_{eq} is the equivalent inertia. The equivalent mass includes, besides the mass of the vehicle, the reported mass of all the rotating elements inside the car. The resistance force can be expressed as follows:

$$F_R = \overbrace{k_R W}^{\text{Rolling and Friction}} + \overbrace{c_x (v - v_{\text{air}})^2}^{\text{Areodynamic}} + \overbrace{W \frac{\tan(\alpha)}{\sqrt{1+\tan^2(\alpha)}}}^{\text{Gradient}} \tag{2}$$

where k_R is the rolling resistance coefficient, W is the gravity force, v is the car speed, v_{air} is the air speed, α is the road's slope, and c_x is the aerodynamic coefficient equal to $(1/2)\rho A_f \gamma$: ρ is the air density, A_f is the frontal area, γ is the drag coefficient, and $(\tan(\alpha)/\sqrt{1+\tan^2(\alpha)})$ is the representation of $\sin(\alpha)$ in the function of the slope, the typically given parameter in this application.

The electric motor is connected to the wheels through a transmission system, usually single speed, and the motor's torque (T_e) can be related to the wheel's torque (T_ω) and the driving force (F_T) through the following equation under the assumption of perfect adhesion between the wheels and the road:

$$T_\omega = T_e \eta_t \gamma \Rightarrow F_T = \frac{T_e \eta_t \gamma}{r} \tag{3}$$

where η_t is the efficiency of the transmission system, γ is the gear ratio, and r is the wheel's radius.

In the EV application, the gear ratio is usually fixed and it is related with the maximum motor rotating speed ($\omega_{\max}$) that the designer sets for the motor according to the following equation:

$$\gamma = \frac{\omega r}{v} = \frac{\omega_{\max} r}{v_{\max}}. \tag{4}$$

The selection of the motor gearing also depends on the maximum transmitted torque, which is typically demanded in the acceleration phase or at the maximum grade.

The efficiency of the transmission system depends on the value of the gear ratio: the higher this ratio, the lower the efficiency penalizing high-speed designs. This value also depends on the number of meshes and torque per teeth's meshing point.

Considering: 1) the dynamic model of the car; 2) the ones of all the resistive forces; and 3) the one of the traction force, it is possible to write the dynamic model of the vehicle as follows:

$$\frac{dv}{dt} = \frac{1}{m_{\text{eq}}} \left[\frac{T_e(v) \eta_t \gamma}{r} - k_R W - \frac{\tan(\alpha)}{\sqrt{1+\tan^2(\alpha)}} W - c_x (v - v_{\text{air}})^2 \right]. \tag{5}$$

The electric motor is typically able to provide a constant torque versus speed up to the point that corresponds to its base speed ω_b, at vehicle speed v_b; from this point forward, the machine works in flux weakening mode, which is characterized ideally by a constant power versus speed. The electric motor requirements, such as maximum speed, base speed, maximum torque, and maximum power at maximum speed, depend on the vehicle's dynamics, as described in the following.

The main vehicle parameters are the maximum speed ($v_{\max}$), the related power to reach it $P_e(v_{\max})$, the acceleration time (t_a) from 0 to the reference speed (v_a) (usually 0–100 km/h or 0–60 mi/h), and the overtaking acceleration time (t_{ov}) at high speed (usually from 90 to 120 km/h).

Fixed the vehicle parameters, from (5), it exists different torque functions $T_e(v)$ (6) in function of the base speed of the motor. Hence, considering a constant torque during the speed range 0-v_a, meaning $v_b v_a$; it is possible to compute the minimum constant torque required to reach v_a in t_a. Otherwise, if $v_b < v_a$ is considered, higher torque is demanded to maintain the same average acceleration. Fig. 3 exemplifies the concept by reporting the boundary curves of the family of the $T_e(v)$ functions, limited by the minimum average torque, and the adhesion limit. Concerning the motor power, the motors with torque curves at lower base speeds are able to fulfill the vehicle requirements at lower power, reducing the whole system sizing (i.e., battery power and inverter power)

$$T_e(v) = f(v_b)|_{t_a, v_a, v_{\max}, t_{\text{ov}}}. \tag{6}$$

Hence, two motor sizing approach can be pursued as follows.

1) Minimize the motor torque to achieve the acceleration by increasing the motor power.
2) Minimize the motor power to achieve the acceleration by enhancing the torque at low speed.

Hence, the motor torque to achieve the acceleration to v_a in t_a is minimized by considering a constant torque ($T_{e,C}$) for the whole acceleration time, equal to the minimum average torque needed. It follows that the motor needs to be selected with a base speed at least up to ω_a which corresponds the vehicle speed v_a. With this hypothesis, (5) can be solved in terms of $v_a(t_a)$ and the average torque required can be computed numerically according to the following equation by considering null starting speed and neglecting airspeed and the road grade:

$$v_a(t_a) = \sqrt{\frac{\frac{T_{e,C}\eta_t\gamma}{r} - k_R W}{c_x}} \tanh\left(\sqrt{\left(\left(\frac{T_{e,C}\eta_t\gamma}{r} - k_R W\right)c_x\right)}\frac{t_a}{m_{\text{eq}}}\right). \tag{7}$$

Considering (7), the only unknown term is the electric motor's torque since the other terms (except for γ, which has already been calculated) are imposed by the vehicle's data. However, it is not possible to analytically solve the equation respect to the term $T_{e,C}$, and the solution is computed numerically. $T_{e,C}$ depends on the car parameters, the speed, and the time to reach it. Fixing the speed and the car parameters, it depends on the acceleration time as follows:

$$T_{e,C} = T_{e,C}(t_a). \tag{8}$$

Depending on the vehicle performance, the maximum torque which should be guaranteed by the motor is the one that at low speed allows to move the car with a maximum admitted grade (α_{ls}). The regulation typically sets this value equal to 30%

$$T_{e,\alpha} = \frac{\tan(\alpha_{ls})}{\sqrt{1+\tan^2(\alpha_{ls})}} W \frac{r}{\eta_t \gamma}. \tag{9}$$

After the torque evaluation, it is possible to calculate the power at maximum speed. In this condition, the inertial force can be neglected because of the steady-state conditions, while a typical grade of the routes on which it is expected to reach the maximum speed of the vehicle is included by considering a typical slope α_{typ} at that speed, differently from the one at low speed

$$\frac{T_e(\omega)\eta_t\gamma}{r} = k_R W + \frac{\tan(\alpha_{\text{typ}})}{\sqrt{1+\tan^2(\alpha_{\text{typ}})}} W + c_x v^2. \tag{10}$$

Multiplying each term of the previous expression by the vehicle's speed and considering (4), the motor's power (P_e) is obtained as follows:

$$P_e(v_{\max}) = \frac{k_R W v_{\max}}{\eta_t} + \frac{\tan(\alpha_{\text{typ}})}{\sqrt{1+\tan^2(\alpha_{\text{typ}})}} \frac{W v_{\max}}{\eta_t} + \frac{c_x v_{\max}^3}{\eta_t}. \tag{11}$$

The only unknown term is the power of the motor at maximum speed, whose value can now be computed. Solving (8) numerically and using (11), it is possible to define the limit performance of the motor.

The evaluated machine in this study is the SynRel motor, whose model is described by the following equations [21]. The motor torque depends on the square current (12), while the voltage depends mainly on the speed (13)

$$T = \frac{3}{4} p (L_d - L_q) i^2 \sin 2\varepsilon = \frac{3}{4} p L_q (k-1) i^2 \sin 2\varepsilon \tag{12}$$

$$V = \omega_e i \sqrt{L_d^2 \cos^2\varepsilon + L_q^2 \sin^2\varepsilon} \tag{13}$$

where L_d and L_q are the axis inductances, p is the number of pole pairs, i is the amplitude of the stator current, k is the saliency ratio, ε is the current angle control, and ω_e is the electrical speed.

Due to these expressions, it is possible to compute the flux weakening capabilities, meaning the performance in the constant power working region.

For the computation of the base torque, it is possible to consider the MTPA control algorithm obtaining the following expression of the torque and the base speed, neglecting the saturation and the resistance voltage drop for the sake of simplicity:

$$T_b = \frac{3}{4} p L_q (k-1) i_{\max}^2; \;\; \omega_{e,b} = \frac{V_{\max}}{L_q \cdot i_{\max}} \sqrt{\frac{2}{k^2+1}}. \tag{14}$$

Considering that at the maximum speed, the typical applied control is the maximum torque per voltage (MTPV), in which the current control angle is equal to $\varepsilon = \text{atan}(k)$, it is possible to obtain (15)–(17) for the maximum amplitude of the current at the maximum speed and the value of the torque.

Due to these expressions, it is possible to compute the powers at the maximum speed (18), the power at the base speed (19), and define their ratio (20).

Therefore, the ratio between the power at the maximum speed and the base power (χ_P), in the following referred as power ratio, is inversely proportional to the ratio between the maximum speed and the base one (χ_n), in the following

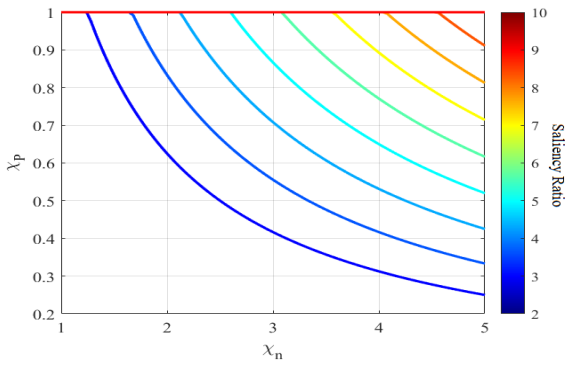

Fig. 4. Flux weakening capability curves in function of the saliency ratio.

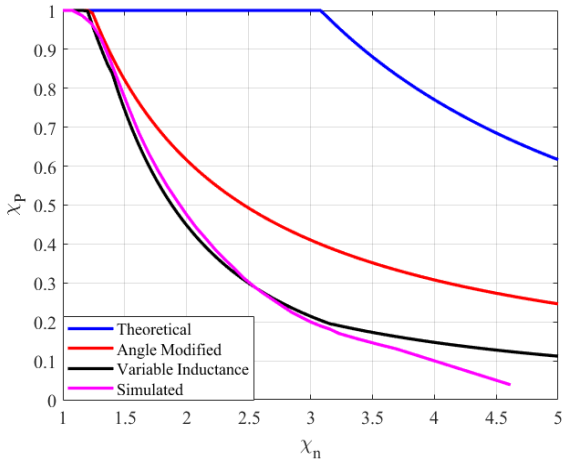

Fig. 5. Flux weakening capability curves: from theoretical to FEM simulated performance.

referred as the speed ratio. These ratios are helpful in comparing the different flux weakening capabilities of the machine and they are reported in Fig. 4 in function of the saliency ratio

$$V_s = L_q i_{\text{fw}} \omega_{e,\max} \sqrt{k^2 \cos^2 \varepsilon + \sin^2 \varepsilon}$$
$$\Rightarrow V_s = L_q i_{\text{fw}} \omega_{e,\max} k \sqrt{\frac{2}{1+k^2}} \tag{15}$$

$$i_{fw} = \frac{V_b}{L_q \omega_{e,\max} k} \sqrt{\frac{(1+k^2)}{2}} \tag{16}$$

$$T_{\text{fw}} = \frac{3}{4} p L_q (k-1) i_{fw}^2 \frac{2k}{k^2+1}$$
$$= T_s = \frac{3}{2} p \cdot \frac{(k-1)}{2k} \frac{V_b^2}{L_q n_s^2} \tag{17}$$

$$P_b = T_b \frac{\omega_{e,b}}{p} = \frac{3}{4}(k-1) \cdot \sqrt{\frac{2}{k^2+1}} \cdot V_{\max} \cdot i_{\max} \tag{18}$$

$$P_{fw} = T_{fw} \frac{\omega_{e,\max}}{p} = \begin{cases} \frac{3}{2} \frac{(k-1)}{2k} \frac{V_b^2}{L_q n_s}, & \text{if } i_{fw} < i_{\max} \\ P_b, & \text{otherwise} \end{cases} \tag{19}$$

$$\chi_P = \frac{P_{\text{fw}}}{P_b} = \begin{cases} \frac{V_b}{L_q \omega_{e,\max} i_{\max}} \sqrt{\frac{k^2+1}{2k^2}} \\ = \frac{k^2+1}{2k} \frac{1}{\chi_n}, & \text{if } i_{\text{fw}} < i_{\max} \\ 1, & \text{otherwise.} \end{cases} \tag{20}$$

While considering the machine voltage limits in Fig. 4, other nonideal behavior affects the flux weakening capability of the SynRel. The poor flux weakening capability of the SynRel is mainly because the voltage limit ellipse has the center coincident with the center of d–q-axis current. With the increase of speed, the ellipse limit area is reduced to fall into the current circle limit. The reduction of the maximum admitted current (for voltage limitation) leads to the reduced available power of the machine. This problem could be partially compensated with an increase in the saliency ratio of the machine, as shown in Fig. 4. The increase of the saliency ratio increases the ratio of the ellipse axes, avoiding falling into the circle. The possibility of increasing the machine's saliency ratio is limited by the presence of the inner ribs in high-speed applications (inserted for mechanical reasons). The saliency ratio is affected especially in the flux weakening, mainly due to the nonsaturation of these ribs with a consequent increase of the quadrature axis inductance. Another important aspect is the MTPA angle control at the base speed. If the angle is much higher than the theoretical one (45°), the flux reduction, which can be possible with the flux weakening while maintaining the same maximum current, is lower with a consequent decrease of the available power. These two effects are more visible in high power density machine, because at the maximum motor current, the saturation of the machine is high both in the rotor and in the stator; it follows that the control angle can reach values over 65° in MTPA. The flux weakening capability is affected, and the performance at high speed degrades up to 60%. The effects on the flux weakening motor capability of the mentioned consideration are reported Fig. 5, computed on a reference SynRel motor, [22], where a more detailed performance has been evaluated by finite element model (FEM) simulation.

The flux weakening capability reported in Fig. 5 helps identify which speed ratio and power ratio are feasible with SynRel technology. Hence, from the vehicle requirements in terms of speed and power, it is possible to properly select the most suitable base speed of the motor, as shown in the next section.

III. Case Studies Evaluation

The proposed approach has been evaluated by referring to two different vehicle classes.

1) Premium high-speed vehicle (PHV), powered by a dual high-performance electric motor.
2) City–car vehicle (CCV), powered by a single electric motor.

These two vehicle classes have borderline dynamic performance, meaningful in the evaluation of the capabilities of the SynRels in EV traction applications.

A. Electric Motor for Premium Vehicle (PHV)

Concerning the PHV case study, the Tesla Model 3 Dual Motor has been taken as reference in terms of vehicle parameters and dynamic performance, see [23], [24] (Table II).

TABLE II
PHV PARAMETERS AND PERFORMANCE

Parameter	Unit	Value	Parameter	Unit	Value
Mass (m)	kg	2500	Drag Coefficient (γ)		0.26
Air's Density (ρ)	kg/m^3	1.225	Wheel's Radius (r)	m	0.30
Mass Correction Factor (k_{eq})		1.04	Maximum Slope ($\tan(\alpha_{typ})$)	%	2.8
Rolling Resistance Coefficient (k_R)		0.0054	Maximum Speed (v_{max})	km/h	250
Frontal Area (A_f)	m^2	1.746	Time 0-100 km/h (t_a)	s	4.0

TABLE III
CCV PARAMETERS AND PERFORMANCE

Parameter	Unit	Value	Parameter	Unit	Value
Mass (m)	kg	2500	Drag Coefficient (γ)		0.26
Air's Density (ρ)	kg/m^3	1.225	Wheel's Radius (r)	m	0.30
Mass Correction Factor (k_{eq})		1.04	Maximum Slope ($\tan(\alpha_{typ})$)	%	2.8
Rolling Resistance Coefficient (k_R)		0.0054	Maximum Speed (v_{max})	km/h	250
Frontal Area (A_f)	m^2	1.746	Time 0-100 km/h (t_a)	s	4.0

The tentative requirements for a SynRel-based powertrains are computed accordingly.

Considering the target vehicle speed of 250 km/h, the maximum speed of the motor has been selected at 18 kr/min, with a gear ratio (γ) of 8.15 and transmission average efficiency of 97% [25].

The boundaries on the torque are computed by (7) for what the required accelerating torque is concerned, while the torque at the adhesion limit is computed as proposed by Rill [19]. The vehicle torque is expected to be equally shared between the two motors; it follows that the motor torque at low speed to achieve the acceleration target is between the boundaries of 360 and 413 N·m.

The torque should be higher than 138 N·m for each motor when considering a grade of 30% at low speed; however, the acceleration constraints require higher torque values.

In addition, through (11), it is possible to calculate the required power at maximum speed ($P_{\omega,m}$), which is equal to 155 kW: although considering that two motors are envisioned, each one should guarantee a power of 77.5 kW and a torque at maximum speed ($T_{\omega,m}$) equal to 41 N·m.

Once the boundaries are defined, two motor sizing approaches can be applied by assuming an ideal flux weakening region with constant power capabilities.

1) Constant motoring torque (360 N·m) is considered up to the base speed of the motor (ω_b) selected at 7200 r/min (vehicle speed v_a). The resulting power at base speed (P_b) is up to 270 kW. It follows that the required accelerating torque is minimized.
2) Higher torque at low speed, close to the adhesion limit (413 N·m), is considered to achieve acceleration, while the motor base speed is computed numerically to reduce the maximum power. With a motor base speed of 4000 r/min, the peak power is reduced at 185 kW, minimum ideal value to achieve the target performance.

Therefore, the two sizing methods at the boundaries for the PHV require different torque and power capabilities of the motor, meaning different flux-weakening characteristics. In particular, the method that minimizes the peak power requires a wider constant power region at high speed, difficult to be obtained with SynRel machines.

B. Electric Motor for City–Car Vehicle

Concerning the CCV case study, a Fiat 500e EV has been taken as a reference; the parameters and the required performance of the vehicle are listed in Table III [11]. These data are used for the computation of the electric motor's requirements.

If the target vehicle speed is fixed at 140 km/h, the maximum motor speed has been reduced to 12 kr/min, a speed value close to the state of the art of this kind of vehicle (Table I). It follows a gear ratio (γ) equal to 9.69 computed by (4), with a conceivable transmission efficiency of 96% [25].

Similar to the PHV case study, the boundaries on the torque are computed by (7); it follows the boundary values for the torque of 158 N·m for the required acceleration and 176 N·m for the adhesion limit. The torque should be higher than 141 N·m at the maximum grade of 30% at low speed; however, the acceleration constraints require higher torque values.

The power at maximum speed ($P_{\omega,m}$) results in 24.5 kW (11), while the torque at maximum speed ($T_{\omega,m}$) is equal to 19.5 N·m.

The same sizing approach can be applied in the CCV case study by assuming an ideal flux weakening region with constant power capabilities.

1) Constant motoring torque (158 N·m) is considered up to the base speed of the motor (ω_b), selected at 8750 r/min (vehicle speed v_a). The resulting power at base speed (P_b) is up to 140 kW. It follows that the required accelerating torque is minimized.
2) Higher torque at low speed, close to the adhesion limit (176 N·m), is considered to achieve acceleration, while the motor base speed is computed numerically to reduce the maximum power. With a motor base speed of 4600 r/min, the peak power is strongly reduced (minimized) to 85 kW.

C. Selection of the Sizing Method

Two sizing methods in terms of power have been proposed for the PHV and CCV, assuming ideal flux weakening characteristics. Table IV lists the comparison of the sizing torque and power along with the resulting speed and power ratios. By reporting these rations on Fig. 5, it is possible to evaluate the feasibility of the sizing strategy (A) or (B) for the two case studies (Fig. 6).

1) *PHV*: The case (A) is feasible even if at the borderline of the motor characteristics, meaning a challenging design. Contrary, the sizing (B) at the maximum speed is clearly over the power capability of the flux weakening operations.

TABLE IV
PHV AND CCV SIZING APPROACHES

Parameter	Unit	PHV(A)	PHV(B)	CCV(A)	CCV(B)
Maximum Torque ($T_{e,max}$)	*Nm*	360	414	158	176
Maximum Power (P_b)	*kW*	270	185	140	85
Required Power at Maximum Speed ($P_{\omega,m}$)	*kW*	77.5	77.5	24.5	24.5
Base Speed/ max speed	*krpm*	7.2/18.0	4.0/18.0	8.6/12.0	4.6/12.0
Speed Ratio		2.5	4.5	1.4	2.6
Power Ratio		0.28	0.41	0.175	0.28
Selection		Feasible	Unfeasible	Feasible	Preferred

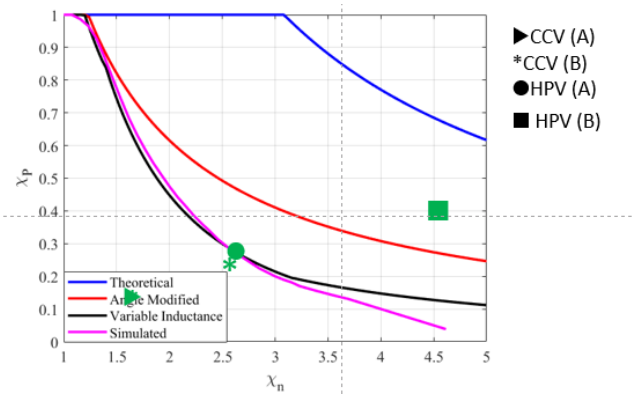

Fig. 6. Sizing method on the flux weakening capability curves.

2) *CCV*: The case (A) is feasible, falling well below the characteristics, but weakly exploiting the motor capabilities. Instead, the solution (B) is close to the limit characteristics, representing a promising sizing avenue.

Hence, it seems confirmed that the sizing method depends on the vehicle performance: the first solution considers the minimization of the torque, while the second solution takes into account the minimization of the power. It is worth remarking that the sizing method B is not feasible for the motor of the PHV due to poor flux-weakening capabilities of the SynRel machine, while it is a feasible sizing avenue for the CCV.

D. Required Performance on a Standard Driving Cycle

Beyond the acceleration and speed capabilities, the electric machine design for EVs needs to be optimized on the driving efficiency, usually evaluated through suitable driving cycles. In this study, the worldwide harmonized light vehicles test procedure (WLTP) cycle 3 [26] has been selected as a reference, representing meaningful driving conditions in urban, extraurban, and highway scenarios. It is one of the most used by automotive companies to compute the vehicle energy consumption.

Due to (4) and (5), it is possible to calculate the torque and the speed working condition of the motor throughout the whole driving cycle in both case studies. In Fig. 7, the driving cycle's points are reported in green, the torque versus speed curve during the motor operation in blue, and the torque versus speed curve during the generator operation in red. Moreover, the

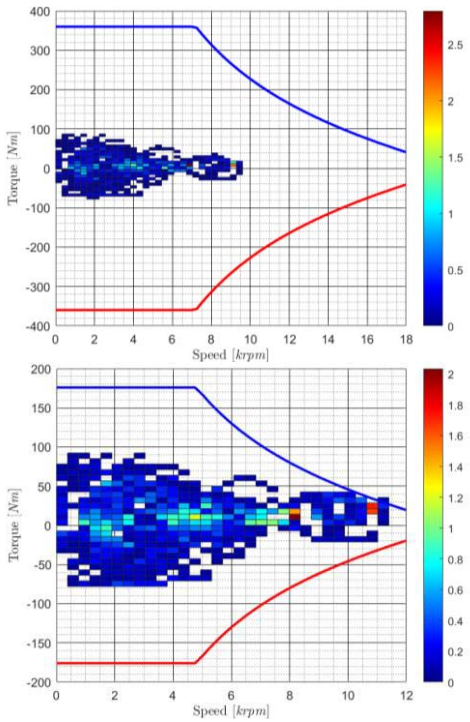

Fig. 7. WLTP 3 operations in torque–speed curves for PHV (above) and CCV (below).

above diagram is referred to PHV car, while the below one is referred to CCV car.

The analysis of the behavior of the motor in the driving cycle can drive the design by selecting the representative working points to evaluate the efficiency and optimize it.

The driving cycles attempt to replicate the statistical adoption of the vehicle, without considering the real maximum performance of the car in terms of acceleration and maximum speed. Therefore, the HPV motor may seem oversized when compared to the considered cycle.

Indeed, the PHV motor works in a low to medium speeds and in a low to medium torque when executing the driving cycle, while the cycle seems more demanding for the CCV motor.

Since the vehicle performance strictly depends on the selected cycle, in the results section, the China light-duty vehicle test cycle for passenger car (CLTC-P) (the reference driving cycle in China) has also been taken into account for the sake of completeness.

IV. DESIGN OF THE SYNREL MOTORS

While the approach for defining the torque speed and power requirements of the motor has been proposed, other requirements, such as size, volume, voltage, and current ratings, are usually defined considering market needs, available power electronics, and battery technologies. In this article, the European Project H2020 ReFreeDrive [10] framework has been taken as a reference for these requirements, respectively, resumed in Tables V and VI, for the PHV and CCV.

The same stator and rotor geometry is supposed aiming to a scalable design, whether the stack lengths and number of winding conductors per slot can be varied. In the requirements,

TABLE V
REQUIREMENTS OF THE PHV SYNREL MOTOR

Parameter	Value	Parameter	Value
DC Voltage	800 *V*	Torque @ Base Speed	≥ 360 *Nm*
Phase Current (Peak Torque)	≤ 820 *A*	Base Speed	≥ 7.2 k*rpm*
Specific Peak Power	≥ 4.3 *kW/kg*	Power @ Base Speed	≥ 270 *kW*
Specific Peak Torque	≥ 8.2 *Nm/kg*	Torque Ripple	≤ 15 %
Stack Length	≤ 202 *mm*	Power @ Max. Speed	≥ 77.5 *kW*
Stator Outer Diameter	≤ 220 *mm*	Maximum Speed	18000 *krpm*
Active Parts' Weight	≤ 47 *kg*	Peak Efficiency	≥ 96 %

TABLE VI
REQUIREMENTS OF THE CCV SYNREL MOTOR

Parameter	Value	Parameter	Value
DC Voltage	800 *V*	Torque @ Base Speed	≥ 360 *Nm*
Phase Current (Peak Torque)	≤ 820 *A*	Base Speed	≥ 7.2 k*rpm*
Specific Peak Power	≥ 4.3 *kW/kg*	Power @ Base Speed	≥ 270 *kW*
Specific Peak Torque	≥ 8.2 *Nm/kg*	Torque Ripple	≤ 15 %
Stack Length	≤ 202 *mm*	Power @ Max. Speed	≥ 77.5 *kW*
Stator Outer Diameter	≤ 220 *mm*	Maximum Speed	18000 *krpm*
Active Parts' Weight	≤ 47 *kg*	Peak Efficiency	≥ 96 %

a value less than 15% for the torque ripple has been selected, considering that the solution will be skewed for the PHV motor. In this way, the final torque ripple should be much lower than this value. This consideration has been made to simplify the optimization process, making it possible to adopt the 2-D FEM for the simulation of each point.

The optimization of the stator and rotor cores has been focused on the PHV SynRel motor, where the challenging requirements and the high rotating speed need the adoption of proper design techniques to reach the performances and guarantee the rotor mechanical integrity [27], [28], [29]. About the design refinement, in the literature, there are several multiobjective derivative-free algorithms matching with the problem of electrical machine optimization [30], [31]. Some of these methods consider the preferences of the decision maker in relation to the choice of the targets: for example, they consider if an objective function should be preferred respect to another one. In the electrical machine context, there is usually a tradeoff between a small torque profile variance (minimization of the torque ripple) and a high value of the mean torque. The local derivative free algorithm used in this work is the DFL algorithm, proposed in [32] and tested on a SynRel in [33].

A. Electric Motor for High-Performance Vehicle (PHV)

Characterization tests on the selected electrical steel were carried out to obtain magnetic properties of the material and to account for manufacturing effects. These material characteristics have been used in the optimization steps and in the performance estimation of the machine. In the preliminary design of the motor, the choice of the number of poles, slots, and barriers is investigated; several preliminary designs were carried out by using typical sizing procedure [34], [35], [36], [37], [38], [39]. For the analyses and the further optimization of the barrier shape, the fluid-shaped barriers (based on the Joukosky equation) have been selected. This barrier shape that has the same path of the d-axis flux allows to maximize the d-axis inductance, while minimizing the q-axis one. Being an optimized curve, the number of variables for the complete optimization can be reduced compared to the other barrier shapes. From these first evaluations, three solutions have been identified and chosen for further optimization, and details of the preliminary design were presented in [40]. The best candidates found have the following parameters:

1) 4 poles, 36 slots, and 4 barriers and a notch;
2) 6 poles, 54 slots, and 4 barriers and a notch;
3) 8 poles, 75 slots, and 4 barriers and a notch.

Starting from these designs, the optimization of the machines (including the stator and rotor variables) has been carried out in order to refine the geometry. Preliminarily, the optimization does not take into account the degrading effects on the performance of the inner rib insertion.

For this analysis, four operating points have been considered.

1) *P1*: The peak torque at base speed.
2) *P2*: The maximum power at the maximum speed.
3) *P3*: The estimated maximum efficiency point (considered referring to 33% of the maximum torque and to 50% of the maximum speed).
4) *P4*: Low torque and low-speed working region to enhance efficiency on the WLTP3 cycle.

TABLE VII
CONSTRAINTS AND OBJECTIVE FUNCTION

Constraint	Unit	Value	Constraint	Unit	Value
Torque @ P1	*Nm*	≥ 400	Ripple @ P1	%	≤ 15
Speed @ P1	*rpm*^{3}	7200	Ripple @ P2	%	≤ 20
Speed @ P2	*Nm*	18000	Efficiency @ P1	%	≥ 97
Torque @ P3	*rpm*^{3}	≈ 140	Efficiency @ P2	%	≥ 95
Speed @ P3	*Nm*	9000	V_{ph} @ All Ps	*V*	≤ 400
Torque @ P4	*rpm*^{3}	≈ 20	**Objective Function**		
Speed @ P4	*Nm*	2000	Maximization of Torque @ P2		

The constraints related to the torque ripple have been chosen equal to the ones of the requirements because the introduction of the inner ribs could increase the torque ripple of the machine but, in order to further reduce it, asymmetric rotor layouts can be adopted. The constraint related to the efficiency in P3 has been increased, as well as the one of the peak torque at base speed and the one of the base speed itself. These margins are useful to satisfy the requirements once that the inner ribs are inserted within the flux barriers (this reduces the motor performance).

For the objective function, it has been decided to use the maximum torque at maximum speed, which is the most critical value because it is where the performance is mainly affected by the inner ribs.

The performance of the proposed solutions is listed in Table VIII (the best performances are highlighted in bold).

TABLE VIII
PERFORMANCE OF THE PRELIMINARY DESIGNS

Performance	Unit	4-pole design	6-pole design	8-pole design
Torque @ P1	*Nm*	410	410	410
Power @ P2	*kW*	94	**110**	78
Torque @ P3	*Nm*	139	139	141
Torque @ P4	*Nm*	20	21	21
Ripple @ P1	%	**14**	15	**14**
Ripple @ P2	%	20	20	20
Efficiency @ P3	%	**97.3**	97.2	97.1
Efficiency @ P4	%	95	95	95

Fig. 8. Stator's and rotor's cross section of the optimized size-pole design.

The three solutions have similar results in terms of torque in P1 and torque ripple; the four-pole design presents the best efficiency value in P3, but the six-pole one has the highest torque production at maximum speed; hence, it has been chosen for further optimizations. It is worth noting that the two solutions (four and six poles) match only with the minimum shaft diameter possible for the application (40 mm), in case of higher shaft diameter, the eight poles solution must be selected. Fig. 8 shows the stator and rotor shape.

The following design step addresses the definition of the inner ribs, meaning the selection of the following parameters: the rib number, the rib position, and their width and inclination. Topology optimization (TO) has been used on the six-pole design to aid the ribs design [22]. The constraint related to the maximum equivalent von-Mises stress in the rotor has been selected, considering a safety coefficient of 1.6 (360 MPa) on the ultimate tensile strength of the adopted electrical steel (540 MPa).

The process results in a rotor structure with the following rib distribution: four ribs inside the first and the second barriers, two ribs inside the third barrier, and one rib within the fourth barrier, close to the ribs definition shown in Fig. 9.

Nevertheless, the results of the TO optimize only the mechanical structure of the rotor without considering the electromagnetic performance; therefore, a further refinement of the rotor geometry by means of a magnetostructural optimization is needed to enhance the machine performance.

The magnetostructural optimization process is constrained by the requirements in Table V, including the same mechanical constraint used in the TO. The performance of this optimized

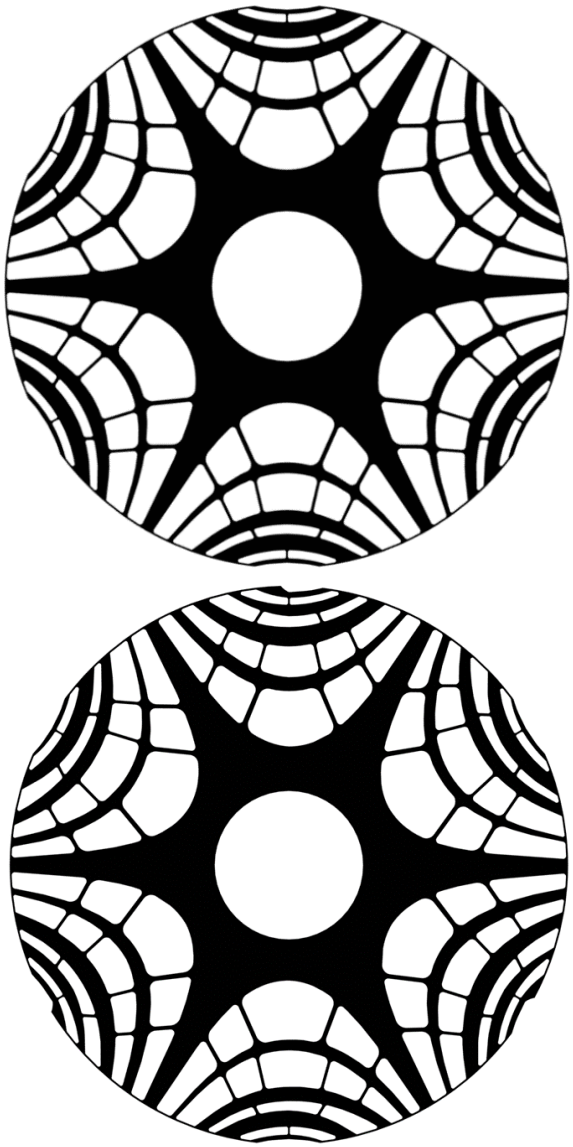

Fig. 9. Rotor shapes of the solutions with inner ribs and symmetric shape (above) and the double asymmetry (below).

TABLE IX
PERFORMANCE OF THE OPTIMIZED TOPOLOGY SOLUTIONS: SYMMETRIC AND ASYMMETRIC ROTOR DESIGN

Performance	Unit	Requirements	Symmetric	Asymmetric
Torque @ P1	*Nm*	≥ 360	**355**	371
Torque @ P2	*Nm*	≥ 41	44	47
Torque @ P3	*Nm*	-	139	140
Torque @ P4	*Nm*	-	21	20
Ripple @ P1	%	≤ 15	**30**	10
Ripple @ P2	%	≤ 20	**40**	19.8
Efficiency @ P3	%	≥ 96	**95.8**	96.04
Efficiency @ P4	%	-	90.9	91

shape is shown in Table IX, while the optimized rotor shape is shown in Fig. 9 (above).

However, despite the heavy optimization step carried out, this last symmetric design has lower performance due to the

presence of the ribs and it does not satisfy some of the requirements, in particular the torque ripple.

Therefore, in attempting to recover adequate torque ripple, a further step featuring asymmetric design has been adopted [41]. Asymmetries in the rotor geometry can be introduced in the following steps.

1) Asymmetries between two poles: proposed in [42], it can be optimized by using the mathematical description of the rotor geometry, and it has a great effect in the ripple reduction of the machine, preserving the same machine behavior in both motoring and generating operations.
2) Asymmetries inside the single pole: proposed in [43], it needs to modify the mathematical description of the rotor geometry. It has effects on the motor ripple but also on the machine performance. This kind of asymmetries can improve the motor performance only in one operating mode (motoring or generating), degrading the performance in the other one.
3) Full asymmetric geometry: detailed in [41], it is a combination of the previous ones. It needs to modify the mathematical description of the rotor geometry and increase the computational burden of the FE analyses. It strongly affects the torque ripple and the performance of the machine; performance improvements are possible in one operating mode.

The full asymmetric geometry has been achieved by performing the step-by-step magnetostructural optimization on the asymmetries 1) and 2), respectively, and then by combining the achieved optimum geometries.

Hence, for the reduction of the torque ripple, the full asymmetric solution, combined with the TO results, has been adopted, and the final design is able to satisfy all the performance requirements in terms of torque, torque ripple, and efficiency.

The performance of the motor is listed in Table IX (the performance not matching the requirements is highlighted in bold), while the final design of the rotor shape is shown in Fig. 9 (bottom). The torque performances of these two solutions are shown in Fig. 10.

The efficiency map (Fig. 11) has been achieved by computing the efficiency of the final design in all the working points. The speed has been extended up to 20 000 r/min to consider overspeed conditions. Considering that overspeed is rarely reached, a safety coefficient equal to 1.2 on the mechanical stress (the maximum stress is 444 MPa) is envisioned as acceptable.

The motor shows good efficiency performance: a wide area is characterized by an efficiency higher than 95%.

Furthermore, the energy results of the WLTP and CLTC-P driving cycle have been obtained with a commercial software [44] (see Table X).

B. Electric Motor for CCV

The SynRel design for the CCV has been obtained by scaling the PHV design: this choice is in the direction of scalability as previously discussed. Therefore, the stack length has been reduced to 95 mm (52.5% lower than the PHV design) and the number of conductors in the slots has been increased. Since the stator and rotor geometries are not modified, the main design aspects are equal to the ones discussed in the previous subchapter. The main differences consist in the values of the peak torque, the base speed, the torque in the flux weakening region, and the maximum speed. The efficiency map reported in Fig. 12 recaps all these values.

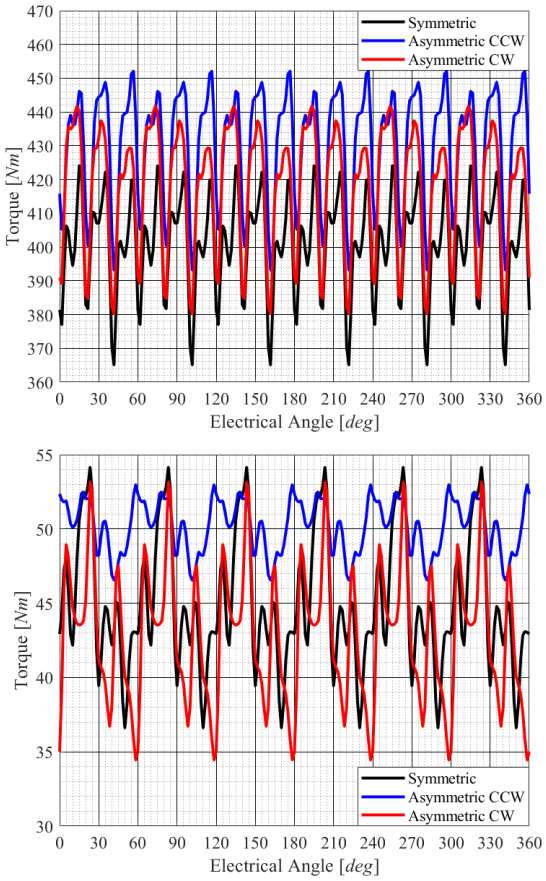

Fig. 10. Torque behavior in the P1 (top) and P2 (bottom) of the symmetric and asymmetric design in CW and CCW.

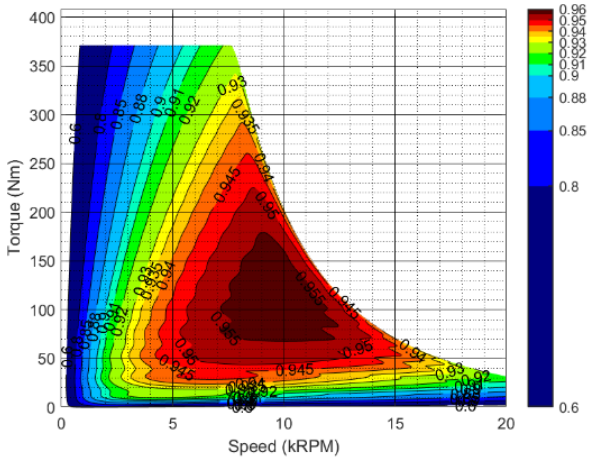

Fig. 11. Optimized double asymmetric topology design: efficiency map (p.u.).

TABLE X
FINAL DESIGN: PERFORMANCES ON THE DRIVING CYCLES

Performance	Unit	WLTP	CLTC-P
Average Efficiency (Energy Use)	%	91.28	90.36
Average Efficiency (Point by Point)	%	87.63	86.26
Electrical Input Energy	*Wh*	3183.9	1770.4
Mechanical Energy	*Wh*	2932.7	1611.9
Electrical Recovered Energy	*Wh*	955.9	752.0
Shaft Generating Energy	*Wh*	1076.4	846.5
Total Energy Losses	*Wh*	371.6	252.2
Energy Losses per km	*Wh/km*	15.97	17.42
Electric Energy per km	*Wh/km*	95.76	70.33

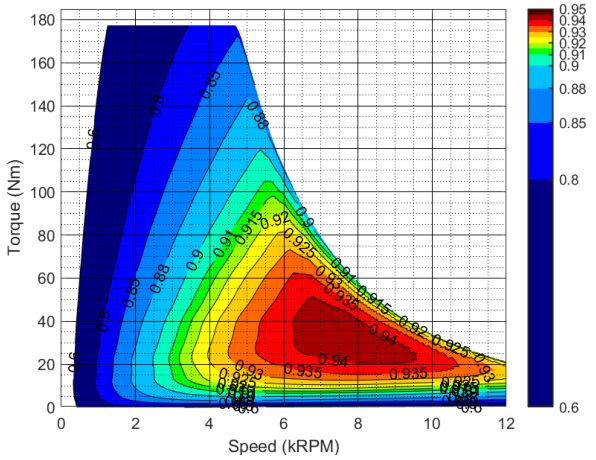

Fig. 12. Scaled version of the optimized solution: efficiency map (p.u.).

TABLE XI
OPTIMIZED SOLUTION: DRIVING CYCLE RESULTS

Performance	Unit	WLTP	CLTC-P
Average Efficiency (Energy Use)	%	92.41	92.21
Average Efficiency (Point by Point)	%	88.94	88.07
Electrical Input Energy	*Wh*	4053.9	2517.6
Mechanical Energy	*Wh*	3758.9	2327.7
Electrical Recovered Energy	*Wh*	1815.5	1369.1
Shaft Generating Energy	*Wh*	1978.4	1491.6
Total Energy Losses	*Wh*	457.8	312.3
Energy Losses per km	*Wh/km*	19.68	21.57
Electric Energy per km	*Wh/km*	96.21	79.32

The energy results of the WLTP and CLTC-P driving cycles is also shown in Table XI. The proposed motor is able to satisfy all the requirements listed in Table VI in terms of torque, power, and power at maximum speed: in fact, the peak torque is equal to 177 N·m, the peak power is equal to 85 kW, and the power at maximum speed is 26 kW.

V. PROTOTYPE MANUFACTURING AND EXPERIMENTAL RESULTS

The final design of the CCV SynRel with no skewed rotor has been manufactured and tested.

The stator and rotor laminations have been prototyped by laser cut and subsequently assembled in a stacked core using the back-lack technology. Meanwhile, the complex rotor geometry has been validated even for punching

Fig. 13. Wound stator core and rotor core of the CCV SynRel.

Fig. 14. Motor prototype.

manufacturing, the envisioned manufacturing avenue for large mass production.

The prototypes' stator windings have been realized with round wires and the motor features a liquid cooling in order to enhance power density. The photographs of the wound stator core and of the rotor core of the CCV SynRel are shown in Fig. 13, while the motor assembly is shown in Fig. 14. The motor prototype with integrated power electronics is shown in Fig. 15.

The motor performance has been validated on a dedicated testbed courtesy of the IFP Energies laboratory Nouvelles (France), as shown in Fig. 16.

The preliminary test made on this machine addresses the verification of the rotor integrity at high speed. For this reason, a no-load strong acceleration and deceleration from 0 to the maximum speed (18 000 r/min) have been made to stress the rotor (Fig. 17). The tests have been repeated several times during which the motor did not produce additional noise or vibration, confirming that the motor is able to reach the maximum speed without mechanical issues in the rotor core.

The test campaign has pointed out promising results about the 75-kW motor with a good match between the experimental

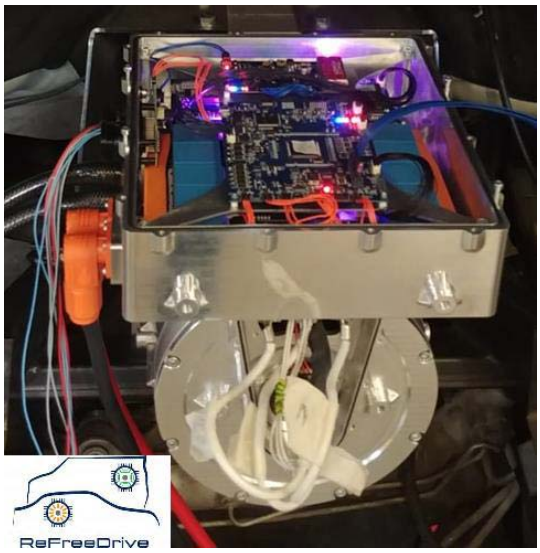

Fig. 15. Power unit.

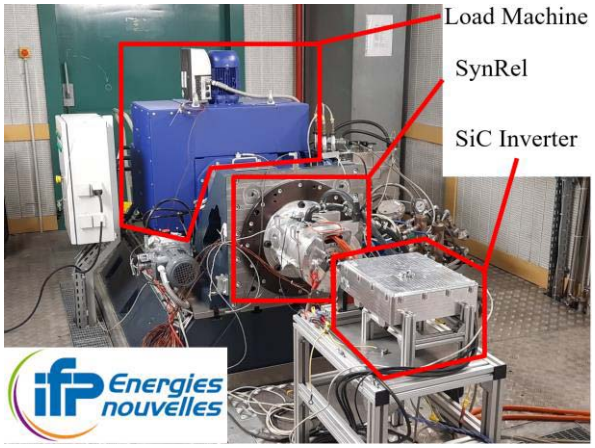

Fig. 16. Test bench in the laboratory of IFP energies Nouvelles (courtesy of IFPEN).

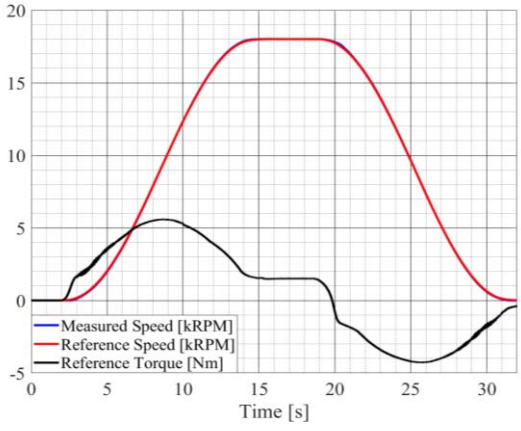

Fig. 17. Experimental acceleration and deceleration phase.

results and the simulation ones; the experimental efficiency map and the comparison between simulations and experimental tests are shown in Fig. 18 and Table XII, respectively.

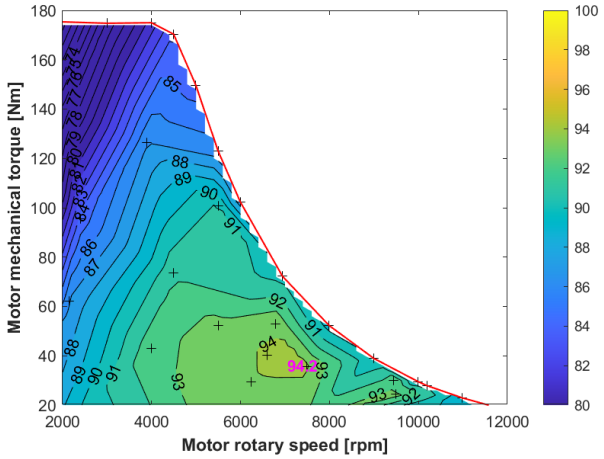

Fig. 18. Experimental efficiency map and comparison between FEM data of the 75-kW solution.

TABLE XII
EXPERIMENTAL VALIDATION OF THE MAIN DATA OF THE CVV 75-kW MOTOR

Performance	Unit	FEM	Tests
Maximum Torque	*Nm*	176.5	176.4
Phase Current	*A*	620	620
DC Voltage	*V*	350	350
DC Current (max)	*A*	300	280
$P_{\omega,m}$	*kW*	26	24
Max. Efficiency	*%*	94.4	94.3
Specific Peak Power	*kW/kg*	4.04	3.9
Specific Peak Torque	*Nm/kg*	8.8	8.7
Peak power density	*kW/l*	14.1	13.6
Peak torque density	*Nm/l*	30	29.9

The maximum torque is equal to 176.4 N·m, nearly equal to the value of the simulation (176.5 N·m). The base speed set for the experiments tests is equal to 4300 r/min, while the one obtained from the simulations is equal to 4600 r/min. The main difference consists in the maximum torque during the flux weakening operations: at maximum speed (12 000 r/min), the maximum torque during the test was equal to 19 N·m (versus 20.5 N·m of the FE analysis) with an output power of 24.0 kW (versus 26 kW of the simulation).

The difference is due to the use of the first flux harmonic for the computation of the efficiency map considering the phase voltages (where a margin of 10% has been imposed to take into account the impact of the harmonics).

The efficiency map and the torque limit curve are in good accordance with the simulations confirming the effectiveness of the adopted machine model tuned by the material characterization. It is worth noting that the minimum tested torque is about 20 N·m, and Fig. 18 reports this value as minimum visible. Despite this, there is a good match between the simulation and experimental results.

Compared to the efficiency map of an RE PM machine, which uses the same boundaries, the SynRel presents a lower maximum efficiency value. The efficiency in the maximum torque area is far lower, but the one in the high-speed region is slightly high. These aspects can be useful for further

consideration, such as adopting the SynRel motor as a low-cost second traction motor. Indeed, when a PM motor works at no-load, the losses at high speed are not zero affecting the system and motor efficiency. Conversely, the SynRel can be easily turned off due to its zero losses at high speed in no-load conditions.

Hence, the SynRel can be used as a second motor to help the car in the high-acceleration cycles while easily turned off to enhance the efficiency otherwise.

VI. Conclusion

This article presents the adoption of a simplified EV model for the definition of the requirements of the electric motor based on the acceleration time and maximum speed of the vehicle. These requirements directly impact on the sizing of the motor power characteristics depending on its flux weakening capabilities. The approach has been detailed for the SynRel technology by proposing an innovative motor design for two borderline case studies: a traction motor for a PHV and a City car.

In this last case study, a prototype has been realized and fully tested; the experimental tests confirm the effectiveness of the design models and related analyses.

The study carried out allows outlining of some general considerations.

The SynRel appears to be a good match for the city electric car (where the motor power can be minimized). Otherwise, when a high-performance EV is considered, the poor flux weakening capabilities of SynRels require an oversizing of the machine in terms of peak power, which could reach high values (about 35% in the proposed case study) compared to other motor technologies with better flux weakening capability. This aspect is more evident when the machine is designed for high speed, where inner ribs are needed in the rotor core for its mechanical integrity. However, by accepting an oversizing of the machine power, it is still possible to satisfy the requirements imposed by high-performance EVs, even if complex design procedures and several optimization steps are needed.

Accounting for efficiency aspects, the cost-effective materials of the SynRel make it less efficient compared to RE PM motors: the increase of the energy losses may result in a reduction of the range of the electric car. Hence, for a comprehensive cost evaluation, the savings achieved with the SynRel technology need to be weighted with the cost of the battery increase required to pursue the same vehicle range.

Another matter of concern of the SynRel technology is the NVH behavior. The functional tests on the prototype did not seem to highlight particular issues; nevertheless, detailed NVH analyses of the proposed solutions will be addressed in future research.

Hence, the SynRel could be a valid alternative to the RE permanent magnet motors in those application where less demanding flux weakening capabilities or reduced efficiency are acceptable. The SynRel weaknesses seem contained in city cars or as second motor in a high-performance dual motor vehicles (in strong acceleration or AWD operations). Indeed, in this last application, there is not an oversizing of the motor, and the poor flux weakening of the machine does not affect the maximum power requirement.

Furthermore, the research on SynRel is ongoing, and new materials and manufacturing process could further enhance the performance of this motor technology.

In a scenario where the RE materials are in shortage and cheaper batteries are available, the SynRel can gain interest as a cost-effective solution for the main traction motor in EV applications.

References

[1] J. Buekers, M. Van Holderbeke, J. Bierkens, and L. I. Panis, "Health and environmental benefits related to electric vehicle introduction in EU countries," *Transp. Res. D, Transp. Environ.*, vol. 33, pp. 26–38, Dec. 2014.

[2] IEA. (2020). *Global EV Outlook 2020*. Paris. [Online]. Available: https://www.iea.org/reports/global-ev-outlook-2020

[3] EU Science Hub—European Commission. (2021). *Materials: A Potential Bottleneck to Deployment of Low-Carbon Technologies in the EU?—EU Science Hub—European Commission*. [Online]. Available: https://ec.europa.eu/jrc/en/news/materials-potential-bottleneck-deployment-low-carbon-technologies-eu

[4] I. Husain et al., "Electric drive technology trends, challenges, and opportunities for future electric vehicles," *Proc. IEEE*, vol. 109, no. 6, pp. 1039–1059, Jun. 2021.

[5] N. Zhao and N. Schofield, "An induction machine design with parameter optimization for a 120-kW electric vehicle," *IEEE Trans. Transport. Electrific.*, vol. 6, no. 2, pp. 592–601, Jun. 2020, doi: 10.1109/TTE.2020.2993456.

[6] L. di Leonardo, M. Popescu, G. Fabri, and M. Tursini, "Performance evaluation of an induction motor drive for traction application," in *Proc. 45th Annu. Conf. IEEE Ind. Electron. Soc.*, Oct. 2019, pp. 4360–4365.

[7] M. Popescu, N. Riviere, G. Volpe, M. Villani, G. Fabri, and L. di Leonardo, "A copper rotor induction motor solution for electrical vehicles traction system," in *Proc. IEEE Energy Convers. Congr. Expo. (ECCE)*, Sep. 2019, pp. 3924–3930.

[8] C. Babetto, G. Bacco, and N. Bianchi, "Synchronous reluctance machine optimization for high-speed applications," *IEEE Trans. Energy Convers.*, vol. 33, no. 3, pp. 1266–1273, Sep. 2018.

[9] N. Bianchi, S. Bolognani, E. Carraro, M. Castiello, and E. Fornasiero, "Electric vehicle traction based on synchronous reluctance motors," *IEEE Trans. Ind. Appl.*, vol. 52, no. 6, pp. 4762–4769, Nov./Dec. 2016.

[10] RefreeDrive. (2021). *Rare Earth Free E-Drives Featuring Low Cost Manufacturing*. [Online]. Available: https://www.refreedrive.eu

[11] EVSpecifications. (2021). *EVSpecifications—Electric Vehicle Specifications, Electric Car News, EV Comparisons*. [Online]. Available: https://www.evspecifications.com

[12] R.-R. Moghaddam and F. Gyllensten, "Novel high-performance SynRM design method: An easy approach for a complicated rotor topology," *IEEE Trans. Ind. Electron.*, vol. 61, no. 9, pp. 5058–5065, Sep. 2014.

[13] A. Credo, G. Fabri, M. Villani, and M. Popescu, "A robust design methodology for synchronous reluctance motors," *IEEE Trans. Energy Convers.*, vol. 35, no. 4, pp. 2095–2105, Dec. 2020.

[14] F. Cupertino, G. Pellegrino, and C. Gerada, "Design of synchronous reluctance motors with multiobjective optimization algorithms," *IEEE Trans. Ind. Appl.*, vol. 50, no. 6, pp. 3617–3627, Nov. 2014.

[15] Y. Wang and H. Fujimoto, "Dynamics control for EVs," in *Modeling, Dynamics and Control of Electrified Vehicles*. Amsterdam, The Netherlands: Elsevier, 2018, pp. 309–337, doi: 10.1016/B978-0-12-812786-5.00009-4.

[16] L. Ray, "Nonlinear tire force estimation and road friction identification: Simulation and experiments," *Automatica*, vol. 33, no. 10, pp. 1819–1833, 1997.

[17] N. K. M'sirdi, A. Rabhi, N. Zbiri, and Y. Delanne, "Vehicle–road interaction modelling for estimation of contact forces," *Vehicle Syst. Dyn.*, vol. 43, no. 1, pp. 403–411, Jan. 2005.

[18] J. Kong, M. Pfeiffer, G. Schildbach, and F. Borrelli, "Kinematic and dynamic vehicle models for autonomous driving control design," in *Proc. IEEE Intell. Vehicles Symp. (IV)*, Jun. 2015, pp. 1094–1099.

[19] G. Rill, *Road Vehicle Dynamics*. Boca Raton, FL, USA: CRC Press, 2012.

[20] G. Genta and A. Genta, *Road Vehicle Dynamics* (Series on Advances in Mathematics for Applied Sciences). Singapore: World Scientific, 2015.
[21] G. Pellegrino, T. Jahns, N. Bianchi, W. Soong, and F. Cupertino, *The Rediscovery of Synchronous Reluctance and Ferrite Permanent Magnet Motors*. Cham, Switzerland: Springer, 2016.
[22] A. Credo, G. Fabri, M. Villani, and M. Popescu, "Adopting the topology optimization in the design of high-speed synchronous reluctance motors for electric vehicles," *IEEE Trans. Ind. Appl.*, vol. 56, no. 5, pp. 5429–5438, Sep. 2020.
[23] D. Gerada, A. Mebarki, N. L. Brown, C. Gerada, A. Cavagnino, and A. Boglietti, "High-speed electrical machines: Technologies, trends, and developments," *IEEE Trans. Ind. Electron.*, vol. 61, no. 6, pp. 2946–2959, Jun. 2014.
[24] MotorWard. (2011). *Tesla Model S Pricing and Specs Revealed*. [Online]. Available: http://www.motorward.com/2011/12/tesla-model-s-pricing-andspecs-revealed/
[25] I. Husain, *Electric and Hybrid Vehicles: Design Fundamentals*. Boca Raton, FL, USA: CRC Press, 2003.
[26] *Global Technical Regulation on Worldwide Harmonized Light Vehicles Test Procedure*, Standard ECE/TRANS/180/Add15, United Nations, 2018.
[27] M. Di Nardo et al., "High-speed synchronous reluctance machines: Materials selection and performance boundaries," *IEEE Trans. Transport. Electrific.*, vol. 8, no. 1, pp. 1228–1241, Mar. 2022.
[28] G. Gallicchio et al., "High speed synchronous reluctance machines: Modeling, design and limits," *IEEE Trans. Energy Convers.*, vol. 37, no. 1, pp. 585–597, Mar. 2022.
[29] M. D. Nardo, G. L. Calzo, M. Galea, and C. Gerada, "Design optimization of a high-speed synchronous reluctance machine," *IEEE Trans. Ind. Appl.*, vol. 54, no. 1, pp. 233–243, Jan. 2018.
[30] A. L. Custódio, J. F. A. Madeira, A. I. F. Vaz, and L. N. Vicente, "Direct multisearch for multiobjective optimization," *SIAM J. Optim.*, vol. 21, no. 3, pp. 1109–1140, 2011.
[31] G. Liuzzi, S. Lucidi, and F. Rinaldi, "A derivative-free approach to constrained multiobjective nonsmooth optimization," *SIAM J. Optim.*, vol. 26, no. 4, pp. 2744–2774, Jan. 2016.
[32] G. Liuzzi, S. Lucidi, and F. Rinaldi, "Derivative-free methods for mixed-integer constrained optimization problems," *J. Optim. Theory Appl.*, vol. 164, no. 3, pp. 933–965, 2015, doi: 10.1007/S10957-014-0617-4.
[33] A. Credo et al., "Design optimization of synchronous reluctance motor for low torque ripple," in *A View of Operations Research Applications in Italy* (AIRO Springer Series). Cham, Switzerland: Springer, 2019, pp. 53–69.
[34] S. Taghavi and P. Pillay, "A sizing methodology of the synchronous reluctance motor for traction applications," *IEEE J. Emerg. Sel. Topics Power Electron.*, vol. 2, no. 2, pp. 329–340, Jun. 2014.
[35] M. Ferrari, N. Bianchi, A. Doria, and E. Fornasiero, "Design of synchronous reluctance motor for hybrid electric vehicles," *IEEE Trans. Ind. Appl.*, vol. 51, no. 4, pp. 3030–3040, Jul. 2015.
[36] G. Pellegrino, F. Cupertino, and C. Gerada, "Automatic design of synchronous reluctance motors focusing on barrier shape optimization," *IEEE Trans. Ind. Appl.*, vol. 51, no. 2, pp. 1465–1474, Apr. 2015.
[37] A. Vagati, A. Canova, M. Chiampi, M. Pastorelli, and M. Repetto, "Design refinement of synchronous reluctance motors through finite-element analysis," *IEEE Trans. Ind. Appl.*, vol. 36, no. 4, pp. 1094–1102, Jul. 2000.
[38] I. Boldea and S. A. Nasar, *The Induction Machines Design Handbook*. Boca Raton, FL, USA: CRC Press, 2010.
[39] J. Pyrhönen, T. Jokinen, and V. Hrabovcová, *Design of Rotating Electrical Machines*. Hoboken, NJ, USA: Wiley, 2009.
[40] A. Credo, G. Fabri, M. Villani, and M. Popescu, "High speed synchronous reluctance motors for electric vehicles: A focus on rotor mechanical design," in *Proc. IEEE Int. Electr. Mach. Drives Conf. (IEMDC)*, May 2019, pp. 165–171.
[41] A. Credo, M. Villani, M. Popescu, and N. Riviere, "Application of epoxy resin in synchronous reluctance motors with fluid-shaped barriers for E-mobility," *IEEE Trans. Ind. Appl.*, vol. 57, no. 6, pp. 6440–6452, Nov. 2021.
[42] N. Bianchi, S. Bolognani, D. Bon, and M. D. Pre, "Rotor flux-barrier design for torque ripple reduction in synchronous reluctance and PM-assisted synchronous reluctance motors," *IEEE Trans. Ind. Appl.*, vol. 45, no. 3, pp. 921–928, May/Jun. 2009.
[43] E. Howard, M. J. Kamper, and S. Gerber, "Asymmetric flux barrier and skew design optimization of reluctance synchronous machines," *IEEE Trans. Ind. Appl.*, vol. 51, no. 5, pp. 3751–3760, Sep./Oct. 2015.
[44] *Motor-CAD*. Accessed: 2022. [Online]. Available: https://www.motor-design.com/motor-cad/

Andrea Credo received the B.Sc. and M.Sc. degrees (Hons.) in electrical engineering with full grade from the University of L'Aquila, L'Aquila, Italy, in 2015 and 2017, respectively, where he is currently pursuing the Ph.D. degree *(cum laudem)* in 2021.

His current research interests include the design and the control of synchronous reluctance motor.

Mr. Credo received the ICEM Jorma Luomi Student Forum Award during the ICEM 2020 in Gothenburg, Sweden (Virtual Conference).

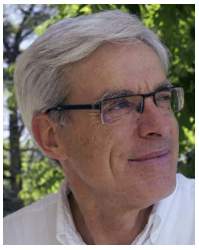

Marco Villani received the M.S. degree in electrical engineering from the University of L'Aquila, L'Aquila, Italy, in 1985.

He became an Assistant Professor of power converters, electrical machines, and drives in 1993. In 1990, he joined the University of Dresden, Dresden, German, as a Research Fellow, and in 1995, he joined Nagasaki University, Nagasaki, Japan. He is currently an Associate Professor of electrical machines design for the degree of Engineering at the University of L'Aquila. He has authored more than 160 technical articles in scientific journals and conference proceedings. His current research interests include modeling and design of electrical machines, optimization techniques for the electrical machines design, and design of permanent magnet (PM) synchronous motors and reluctance motors for industrial, automotive, and aerospace applications.

Giuseppe Fabri (Member, IEEE) received the M.S. degree in electronic engineering and the Ph.D. degree in electrical and information engineering from the University of L'Aquila, L'Aquila, Italy, in 2009 and 2013, respectively.

He is currently a Researcher in the field of power converter, electrical machines, and drives with the Department of Industrial and Information Engineering and Economics, University of L'Aquila. In 2013, he joined the Industrial Electronics Laboratory, Swiss Federal Institute of Technology, Lausanne, Switzerland, as a Research Fellow, where he was involved in the development of a real-time simulator for induction motors. The main research activities concern design, development, control, and test of electrical machines and drives mainly related to fault-tolerant systems for aircraft and automotive applications.

Mircea Popescu (Fellow, IEEE) received the M.Eng. and Ph.D. degrees in electrical engineering from the Politehnica University of Bucharest, Bucharest, Romania, in 1984 and 1999, respectively, and the D.Sc. degree in electrical machines from Aalto University, Espoo, Finland in 2004.

Earlier in his career, he was with Aalto University and also with the SPEED Laboratory, University of Glasgow, Glasgow, U.K. He is currently a Chief Technology Officer with Motor Design Ltd., Wrexham, U.K., a software and consultancy company headquartered in the U.K., with offices in U.S., and has more than 30 years of engineering experience. He has published more than 150 articles and his publications have received three IEEE best paper awards. His consultancy contributions for industry are incorporated in many state-of-the art products. Current major projects include electrical machines and drives for hybrid/electrical vehicles and formula-e racing cars.

Dr. Popescu acted as the Officer of the IEEE Industry Application Society Electrical Machines Committee, from 2010 to 2017.

Open Access funding provided by 'Università degli Studi dell'Aquila' within the CRUI CARE Agreement